# Capacitor-Inspired Metamaterial Inductors

Yue Li[1,2] and Nader Engheta[2,*]

[1]*Department of Electronic Engineering, Tsinghua University, Beijing 100084, China*
[2]*Department of Electrical and Systems Engineering, University of Pennsylvania, Philadelphia, Pennsylvania 19104, USA*

(Received 24 August 2015; published 8 November 2018)

In optical metatronics, where properly designed nanostructures function as lumped optical circuit elements, the capacitive and inductive optical circuit elements are nanostructures with positive and negative real parts of the permittivity of their materials, respectively. Aside from this difference in material properties, other features such as shapes and dimensions of these two elements may be similar. In the rf and microwave domains, however, conventional capacitors and inductors have vastly different features, i.e., one is made of parallel plates and the other is formed by wound wires. Here, inspired by optical metatronics, we propose to bring the notion of optical metatronics back into the low-frequency domain, by suggesting a capacitorlike structure that behaves as an inductive circuit element at microwave frequencies. This simple design may be achieved by adding certain sidewalls in the capacitor structure, and thus its shape is different from conventional inductors made of wires and spirals. The approximate range of inductance can be conceptually evaluated using relations analogous to those of the capacitance. Using numerical and analytical methods, we determine its complex impedance and quality factor as a function of frequency and all the dimensional parameters involved. From this analysis, we find that as compared with a conventional inductor this structure may have certain advantages, which include a higher quality factor due to its approximately closed structure and strong dependence of its inductance value on its height with weaker dependence on its cross section. We also study a subwavelength resonator using our proposed structure as its inductive element, confirming its performance numerically.

DOI: 10.1103/PhysRevApplied.10.054021

## I. INTRODUCTION

Lumped circuit components, e.g., inductors, capacitors, resistors, diodes, etc., have been important building blocks in the development of rf and microwave electronics over the past several decades. Electronic circuits can be readily designed by different combinations of these elements, providing an excellent connection between the modularity and simplicity of circuit architecture. Of these lumped components, inductors and capacitors are the ones that effectively store energy, causing the desired response in the frequency domain. However, it is well known that in the rf and microwave domains, the physical and operating principles behind the conventional inductors and capacitors are different [1]. Specifically, the capacitor stores the electric energy in the form of electric field due to the charge accumulation on their conducting plates, and thus the phase of its current is 90° ahead of its voltage phase, while the inductors store magnetic energy in the form of magnetic field resulting from the current flow in their wires, and due to the Faraday law of induction the current is 90° behind the phase of the voltage. A typical capacitor is made of two parallel conductors, and a standard inductor is formed by a set of wound wire [2–4] or spiral strips [5–10]. Over many decades, various theoretical models have been studied to analyze the energy storage and dissipation of such well-known elements.

However, in the field of optical metatronics, which addresses the optical lumped circuit elements at the nanoscale [11–14], a close relationship and analogy exists between the optical inductors and optical capacitors formed by subwavelength nanoparticles [11,12]. For example, the plasmonic nanoparticles with negative permittivity ($\epsilon < 0$) operate with optical impedance resembling the impedance of an inductor (when the dispersion of permittivity is taken into account), and the nonplasmonic (e.g., dielectric) nanoparticles with positive permittivity ($\epsilon > 0$) operate as capacitors [11,12]. Aside from this difference in material properties, other features such as shape and dimension of these two metatronic elements may be similar. With the identical dimension and absolute value of permittivity for both particles, the magnitude of the reactance of the optical inductor is equal to the reactance magnitude of the optical capacitor. That is to say, by changing the sign of permittivity of a lossless

*engheta@ee.upenn.edu

 © 2018 American Physical Society

nanoparticle, an inductor can be changed to a capacitor with the same reactance magnitude (but of course a different phase). For deeply subwavelength nanoparticles, the electric fields and the electric displacement currents inside the nanoinductors and nanocapacitors are approximately uniformly distributed, but the phase between them is determined by the sign of the permittivity [15]. Similarly to the lumped circuit elements in rf and microwave wavelengths, in the paradigm of optical metatronics, the subwavelength nanoparticles also exhibit the lumpedness property at the operating optical frequencies. Complex circuits with desired functionalities, e.g., optical nanofilters [13,14] and matching circuits for nanoantennas [16,17] can be designed in the analogous way as in the rf and microwave. From the above discussion, we restate that in the optical metatronics, the lumped optical inductors and optical capacitors behave with the analogous principle involving the electric field and electric displacement currents, whereas in the rf and microwaves, the conventional inductors and capacitors follow separate principles.

Here in the present work, we aim to bring the notion of optical metatronics back into the low-frequency domain and to transplant the operational similarity between the optical inductors and optical capacitors in the optical metatronics into the rf and microwave domains, by designing microwave inductors based on the structure of a microwave capacitor, thus coining the term of capacitor-inspired metamaterial inductors.

## II. CAPACITOR-INSPIRED METAMATERIAL INDUCTORS

Figure 1(a) shows a typical rf and microwave capacitor, which consists of two parallel metallic plates (denoted by yellow) and an internal dielectric with positive permittivity (depicted by green). The impedance of the capacitor is $Z = d/(-i\omega\epsilon A)$, a well-known expression in terms of the distance between two plates ($d$), the area of the plates ($A$), and the permittivity of the dielectric ($\epsilon$). (We use the time harmonic convention $e^{-i\omega t}$.) As illustrated in Fig. 1(b), a filling material with negative permittivity (depicted by blue) is inserted instead, which causes the phase of the current to be 90° behind the voltage, different from the phase of the current in Fig. 1(a), which is 90° ahead of the voltage. Therefore, with the proper dispersion of the permittivity taken into account the capacitor in Fig. 1(b) is operating as a lumped inductor, analogous to the plasmonic nanoparticles as optical inductor in metatronics [11,12]. In the rf and microwave regimes, however, it is challenging to find a material with negative permittivity that is easily insertable between the two metallic plates in Fig. 1(b). The guided-wave structures [18,19] may provide an alternative platform for achieving effectively negative permittivity in rf and microwave [18,19]. For example, a parallel-plate waveguide (PPW) made of perfectly electric conducting

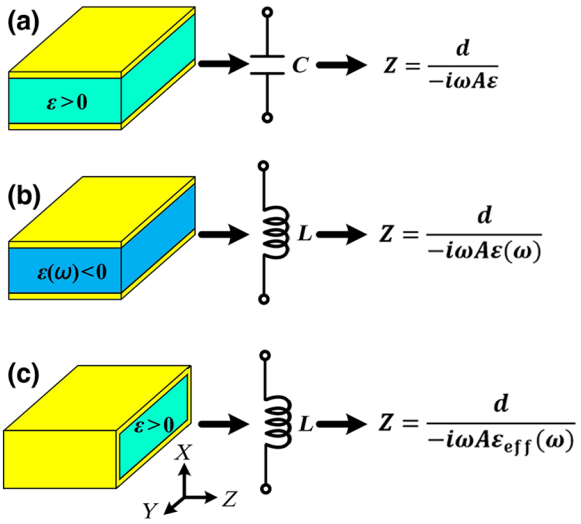


FIG. 1. Concept of capacitor-inspired metamaterial inductors. (a) A standard capacitor in rf and microwave, using two parallel metallic plates and a filling dielectric with positive permittivity. (b) An element with inductive impedance based on (a), by assuming a filling material with negative permittivity. (c) Our proposed structure for (b), which is based on (a) when two metallic side walls are added at the two ends parallel with the $x$-$z$ plane. This structure functions with inductive impedance.

(PEC) walls and filled with a conventional dielectric, when operated with a transverse electric (TE) mode $TE_{10}$ below its cutoff frequency, may behave as a structure with negative effective permittivity [18,19]. The effective relative permittivity ($\epsilon_{\text{eff}}$) of this structure exhibit the Drude-type dispersion, expressed as $\epsilon_{\text{eff}} = \epsilon_{\text{act}} - \pi^2 c^2/(\omega^2 a^2)$, where $\epsilon_{\text{act}}$ is the actual relative permittivity of the filling dielectric, $\omega$ is the operating angular frequency, $c$ is the vacuum speed of light, and $a$ is distance between two PEC parallel plates [18,19]. When the waveguide operates below its cutoff frequency, we can effectively achieve epsilon-negative (ENG) structure, using standard epsilon-positive (EPS) material in microwave.

As shown in Fig. 1(c), the new inductor is simply formed by adding two PEC side walls on both sides of the parallel plates of the capacitor, i.e., the two sides that are parallel with the $x$-$z$ planes, shown in Fig. 1(a). For now, the other two sides that are parallel with the $x$-$y$ plane are left open. A voltage difference between the two middle points on the interior top and bottom plates from inside generates an electric field inside the structure, which has to vanish at the two PEC side walls just added. This structure with the subwavelength dimensions, in which a waveguide is effectively formed by the two PEC side walls we just added, is operating at the frequency much below its $TE_{10}$ cutoff frequency, and thus the effective permittivity of the structure is negative. Due to PEC walls parallel with the $x$-$z$ plane, the $x$-oriented electric field varies sinusoidally along the $y$ axis, and evanescently along the $z$

axis. As we show below, this structure effectively acts as an inductive impedance with the phase of the current 90° behind the voltage. This lumped inductor does not have winding wires, and its appearance is similar to a capacitor, except with the two PEC side walls that are added at its two side ends. When the frequency is zero, a conventional capacitor in Fig. 1(a) operates as an open circuit, but the structure in Fig. 1(c) expectedly operates as a short circuit due to the PEC side walls, which agrees with the operation of a typical inductor made of spiral or wound wires.

## III. OPERATING PRINCIPLE AND NUMERICAL DEMONSTRATIONS

As an example of such inductors, in Fig. 2 we discuss the case of the structure utilizing a rectangular waveguide. We start from the typical rf capacitor, illustrated in Fig. 2(a), consisting of two PEC parallel plates with air filling the space between them. Based on the structure of the capacitor, a new inductor is achieved by adding two PEC walls at the side ends as a rectangular waveguide along the $z$ axis, illustrated in Fig. 2(d), with the similar appearance as the capacitor. In order to excite the desired field between the two PEC parallel plates in both cases shown in Figs. 2(a) and 2(d), a PEC post is positioned in the center and a hole is cut from the top PEC plate. Therefore, the capacitor or the inductor can be connected with typical coaxial cables, e.g., the inner conductor of the coaxial cable connects with the center PEC post, and the outer conductor connects with the top PEC plate at the hole. Using the numerical method of the finite integration technique (FIT) (provided by CST Microwave Studio®), we simulate the field distributions inside the capacitor [Fig. 2(a)] and inductor [Fig. 2(d)]. The detailed view of the port setup in the numerical simulation can be seen in the inserted panel of Figs. 2(a) and 2(d). We use a discrete port, e.g., a voltage or current source, to connect to the center PEC post and top PEC plate.

For the typical capacitor in Fig. 2(a), we show a snapshot of distribution of the electric field on the middle mathematical plane, in Fig. 2(b). The inside electric field is almost uniformly distributed with -$x$-axis polarization. After 90° phase difference, the magnetic field with clockwise rotation around the center PEC post is shown in Fig. 2(c). For the new inductor in Fig. 2(d), the snapshots of electric field and magnetic field (90° phase difference) are also illustrated in Figs. 2(e) and 2(f). The magnetic-field vector is also clockwise rotation, but the electric-field vector is $+x$-axis polarized, i.e., 180° phase difference as compared with the electric field inside the capacitor. That is to say, the phase differences between the electric and magnetic fields inside these two structures are $+90°$ and $-90°$ due to the positive and negative effective permittivity, $\epsilon_{\text{eff}}$, inside the two structures shown in Figs. 2(a) and 2(d). Therefore, by adding two PEC side walls at the side ends of a rectangular capacitor, the phase relation between the interior electric and magnetic fields can be changed to make the structure function as an inductive impedance, thus the name capacitor-inspired metamaterial inductor. The detailed dimensions of this inductor are shown in Fig. 3(a), including the width $a$, the length $l$, the height $d$, and the diameter of the top hole $t$. The diameter of the center PEC post is 0.5 mm in the entire study. [In Fig. 3(a) the top plate has been moved upward in order to clearly show the dimensions]. As a basic model of this inductor, we select $a = l = 10$, $d = 1$, and $t = 1$ mm. The calculated impedance phase of the basic model is uniformly $-90°$ in the frequency range from 100 to 1000 MHz, exhibiting an inductor response, as shown in Fig. 3(b).

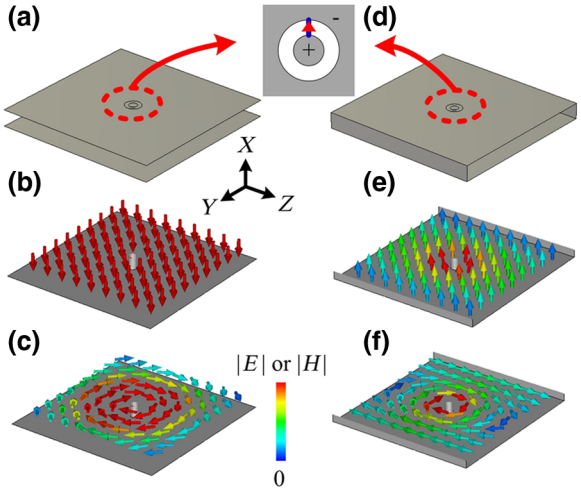


FIG. 2. Field distributions in our proposed structure as compared with those in a conventional capacitor. (a) Conventional rf and microwave capacitor with two PEC parallel plates. Snapshots of (b) the electric field and (c) the magnetic field distributions in the middle mathematical plane between the PEC parallel plates, with the 90° phase difference between the two snapshots. (d) Our proposed structure of the capacitor-inspired metamaterial inductor. Snapshots of (e) the electric-field and (f) the magnetic-field distributions in the middle mathematical plane inside the inductor, with 90° phase difference between the two snapshots. Enlarged view of the port connection on the top PEC plate of the inductor in (a) and (d).

In our numerical simulations presented here, however, we assume the walls to be PEC for the sake of simplicity in introducing the concept while the radiation leakage due to the open sides of the structure is taken into account. In Fig. 3(c), we present the effects of the wall loss in our findings. The loss in the inductor comes from two sources: the first one is the metallic loss due to the finite conductivity of the walls, and the second one is the radiation leakage at the open boundaries. Here, we use the basic model, as an example, to analyze the effects of loss on the performance of our proposed structure. Four different cases are studied

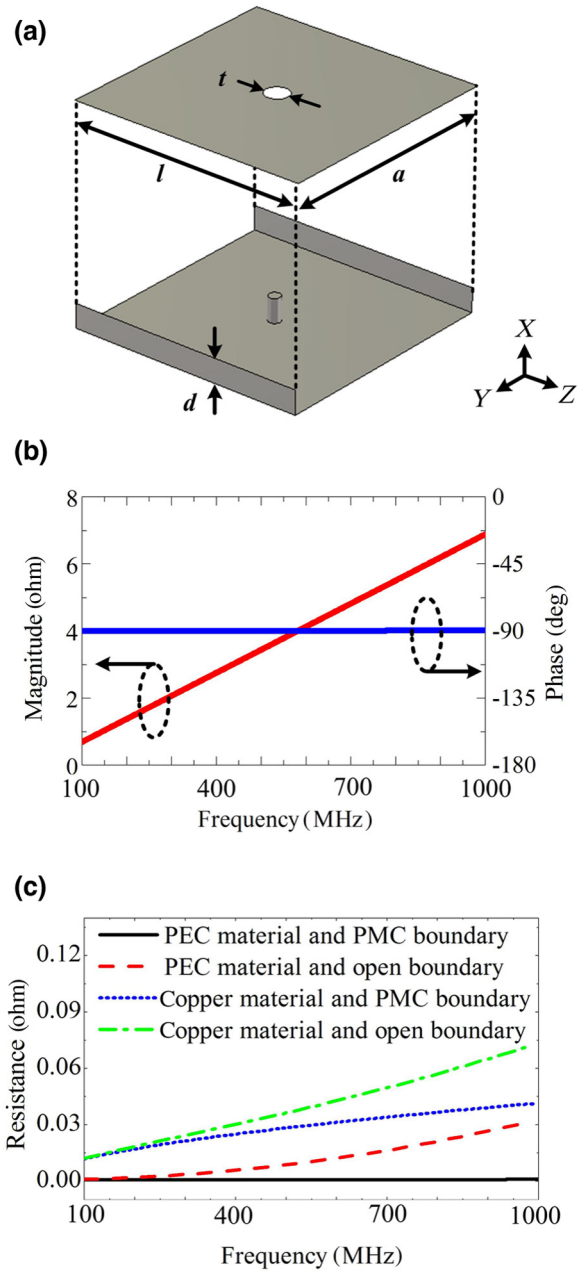


FIG. 3. Simulation results of the basic model of proposed inductor. (a) The geometry and the dimensions of the inductor of Fig. 2(d). The top plate has been removed in order to show the details of interior geometry. (b) The simulated magnitude (red curve) and phase (blue curve) of the impedance of the basic model with dimensions $a = l = 10$, $d = 1$, and $t = 1$ mm. (c) Simulation results for the equivalent resistance (due to the wall loss and radiation leakage) of the basic model with different materials and different boundaries.

and compared: (1) The structure is made of PEC material for the metallic walls and perfect magnetic conductor (PMC) for the open boundaries in the waveguide, so no loss is present; (2) The structure is made of PEC material for the metallic walls and actually open boundary at the waveguide's open ends, so the only loss is the radiation loss; (3) The structure has copper ($\sigma = 5.96 \times 10^7$ S/m) for the metallic walls and PMC boundary at the waveguide's open ends, so the only loss is in the metallic walls; (4) The structure is made of copper for the metallic walls and open boundary at the waveguide's open ends, so both metallic loss and radiation loss are present. All these cases are presented in Fig. 3(c). As shown in the black curve, the equivalent resistance is zero in the no loss case. When we have the open boundary (instead of using PMC) at the open ends, the evanescently decaying field is not zero at the open boundary and thus leaks out. At a higher frequency, the operating frequency is closer to the cutoff frequency and thus we have a smaller decay rate of the evanescent wave, causing more energy leakage at the open boundary. When we have copper for the metallic walls, and PMC for the open ends, at higher frequencies, we have more material loss. Finally, we have both copper as the metallic walls and open boundary for open ends, both losses are present as clearly noticed in the figure. In practical scenarios, the loss, including the metallic loss in the walls and radiation loss from the two open sides of this structure is inevitable.

The mode of interest in this rectangular waveguide is the first-order transverse electric (TE) mode, e.g., $TE_{10}$ mode. The magnitude and phase distributions of $E_x$, $H_y$, and $E_z$ are shown in Fig. 4. By adding the PEC walls at the two side ends of a standard capacitor, the electric field of the $TE_{10}$ mode is established in the $x$-$y$ plane. The new structure operates with a deeply subwavelength dimension ($a \ll \lambda$), and therefore the rectangular waveguide itself operates below its cutoff frequency, and the electric field is evanescent in the $x$-$z$ plane. As shown in Fig. 4(a), the electric field varies to zero at the PEC ends along the $y$ axis, and is evanescent along the $z$ axis. The length of the structure is also subwavelength, e.g., much smaller than the operating wavelength. The electric field is unable to completely drop to zero at the open ends along the $z$ axis, causing small energy leakage. The magnetic-field components $H_y$ and $H_z$, shown in Figs. 4(b) and 4(c), vary along the $y$ and $z$ axes as expected from the standard $TE_{10}$ mode. The phase distributions of three components are plotted in Figs. 4(d)–4(f). The phase of $E_x$ is uniform with 90°difference from the phase of the magnetic components $H_y$ and $H_z$, consistent with the $TE_{10}$-mode scenario.

Next, we evaluate the key quantities of such a capacitor-inspired metamaterial inductor using theoretical and numerical analysis. We start from the impedance of the capacitor in Fig. 1(a). For the sake of simplicity and clarity of the concept, we first ignore the material loss in the wall and the filling dielectric. We have

$$Z = \frac{d}{-i\omega A\varepsilon}. \tag{1}$$

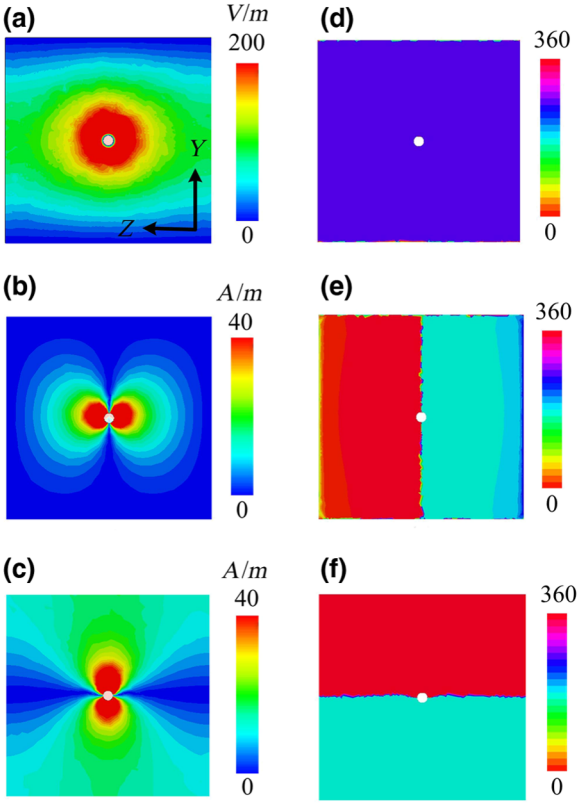


FIG. 4. Field distributions on the middle mathematical plane of the proposed structure in Fig. 2(d). Magnitude distributions of (a) $E_x$, (b) $H_y$, and (c) $H_z$. Phase distributions of (d) $E_x$, (e) $H_y$, and (f) $H_z$.

(Due to the fringing fields, the impedance may be slightly different from what is obtained from (1) depending on the specific dimensions.) Then, we use effective relative permittivity ($\epsilon_{\text{eff}}$) of the waveguide instead of the actual relative permittivity ($\epsilon_{\text{act}}$), and we get

$$Z=\frac{d}{-i\omega A\varepsilon_0\varepsilon_{\text{eff}}}=\frac{d}{-i\omega A\varepsilon_0[\varepsilon_{\text{act}}-\pi^2c^2/(\omega^2a^2)]}\equiv -i\omega L. \tag{2}$$

Therefore, the equivalent inductance is expressed as

$$L\equiv\frac{Z}{-i\omega}=-\frac{d}{\omega^2A\varepsilon_0\varepsilon_{\text{eff}}}=-\frac{d}{\omega^2A\varepsilon_0[\varepsilon_{\text{act}}-\pi^2c^2/(\omega^2a^2)]}. \tag{3}$$

Therefore, the impedance can be expressed as a function of frequency ($\omega$) and dimensions ($a$, $l$, and $d$). When operating angular frequency satisfies $\varepsilon_{\text{act}}\ll\pi^2c^2/(\omega^2a^2)$, the equivalent inductance can be expressed approximately as a constant:

$$L\approx\frac{da^2}{\varepsilon_0\pi^2c^2A}. \tag{4}$$

When the dimensions of the inductor are deeply subwavelength, i.e., $d\ll\lambda$, $l\ll\lambda$, and $a\ll\lambda$, where $\lambda$ is the free-space wavelength, the effective inductance of this structure is almost a linear function of the height $d$. Due to the sinusoidal and evanescent distribution of the electric field inside the inductor, $A$ should be treated as the effective area of the PEC parallel plates. Then, we utilize the FIT method to calculate the values of impedance, equivalent inductance, and quality factor ($Q$) for given sets of dimensions.

## IV. PARAMETER STUDY AND DISCUSSION

The calculated reactance, equivalent resistance, equivalent inductance, and $Q$ of this capacitor-inspired metamaterial inductor filled with air ($\epsilon_{\text{act}}=1$) are shown in Fig. 5, as a function of frequency and each key dimension. The frequency range in our simulation is 100–1000 MHz (wavelength in free-space ranges from 3 m to 300 mm). $Q$ is defined as [8]

$$Q=|\text{Reactance}|/\text{Resistance}=\text{Im}(Z)/\text{Re}(Z). \tag{5}$$

Figure 5 presents the results of our numerical simulations for the inductor performance in terms of frequency, and each of the dimensions, i.e., width $a$, the length $l$, the height $d$, and the hole diameter $t$. The parametric study is based on the basic model (filled with air, $\epsilon_{\text{act}}=1$) with $l=10$ mm, $a=10$ mm, $d=1$ mm, $t=1$ mm and changing one parameter while the other two are kept fixed. As shown in Fig. 5(a), the magnitude of reactance increases with frequency at a given fixed $a$, in agreement with Eq. (2). For a given frequency, as we increase $a$, two effects occur in Eq. (2): the effective area $A$ increases and the absolute value of $\epsilon_{\text{eff}}$ decreases. From our numerical results, we note that the magnitude of reactance still increases with increasing $a$ at a given fixed frequency. In Fig. 5(b), the equivalent resistance increases with increasing $a$ at a fixed frequency, due to the decrease in the decay rate of evanescent wave along the $z$ axis and consequently more energy leakage at the open side walls. The equivalent resistance also increases with the frequency at a given fixed $a$, because the operating frequency is getting closer to the cutoff frequency, and thus the decay rate of the evanescent wave decreases. In Fig. 5(c), the equivalent inductance, derived from the data in Fig. 5(a), is almost constant vs frequency at a given $a$, in agreement with Eq. (4). As discussed above, the equivalent inductance increases with increasing $a$ at a given frequency, but *not* necessarily linearly. In Fig. 5(d), $Q$ is calculated from the data in Figs. 5(a) and 5(b). $Q$ decreases with increasing $a$ at a given fixed frequency and also decreases with rising frequency at a fixed $a$. With deeply subwavelength dimensions, the quality factor $Q$ of this inductor is in the range $10^2$–$10^5$, much higher than the conventional inductors made of wound wire [2–4] or spiral strips [5–10]. This is one of the advantages of such inductors.

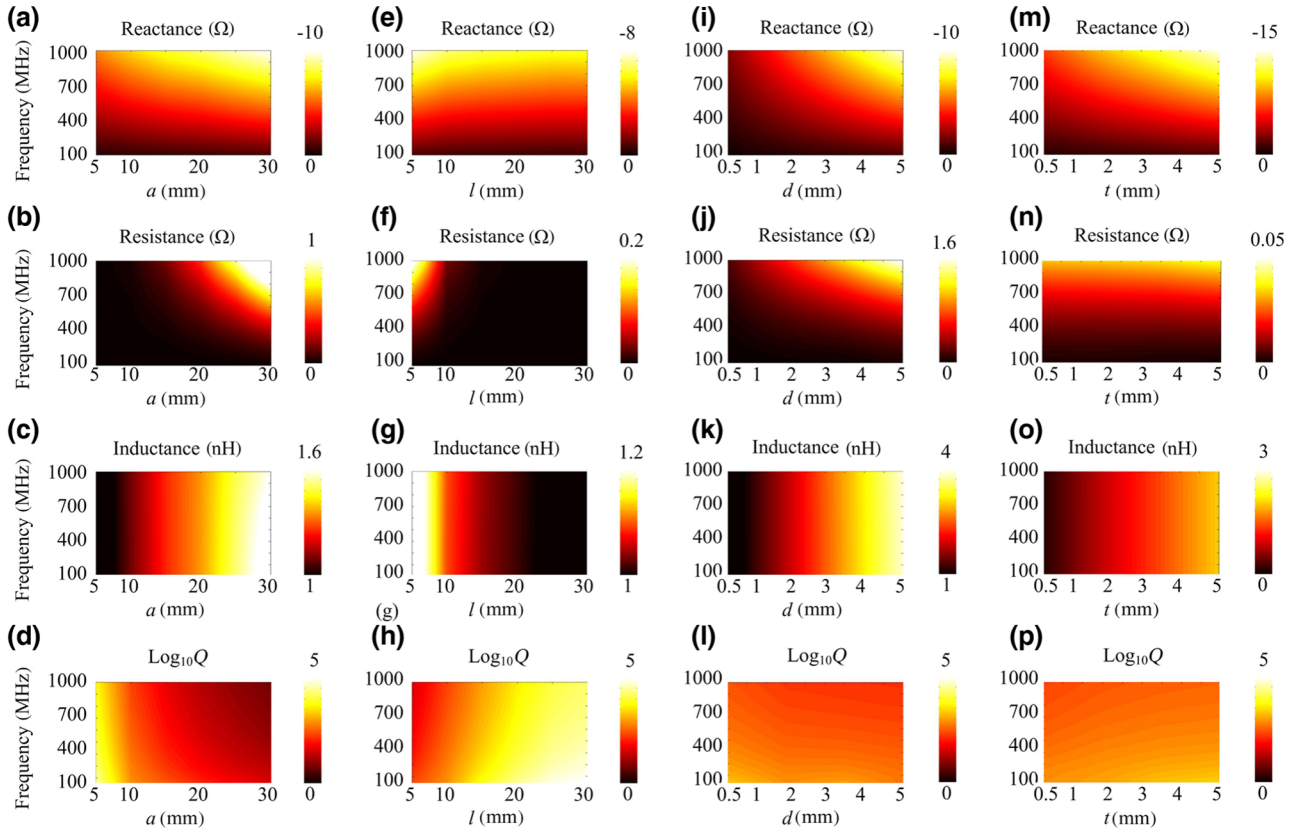


FIG. 5. Simulation results for the parameters of our proposed structure. (a) Reactance. (b) Equivalent resistance. (c) Equivalent inductance. (d) $Q$ as a function of frequency and $a$ (inductor width). (e), (f), (g), and (h) The same as (a), (b), (c), and (d), but as a function of frequency and $l$ (inductor length). (i), (j), (k), and (l) The same as (a), (b), (c), and (d) but as a function of frequency and $d$ (inductor height). (m), (n), (o), and (p) The same as (a), (b), (c), and (d), but as a function of frequency and $t$ (hole diameter).

The reactance and equivalent resistance as a function of frequency and $l$ are illustrated in Figs. 5(e) and 5(f). At a fixed $l$, both the magnitude of reactance and the equivalent resistance increase with increasing frequency, following the similar reasons as mentioned above for $a$. At a fixed frequency, the magnitude of reactance decreases with increasing $l$, due to the increase of the effective area $A$. The electric field drops evanescently as it approaches the open ends. Therefore, $A$ changes little and the reactance also changes little as we increase $l$. The equivalent resistance decreases with increasing $l$, because longer $l$ causes less leakage of energy at the open boundaries. As illustrated in Fig. 5(g), the equivalent inductance is also a constant vs frequency at a given fixed $l$, and decreases with increasing $l$. The calculated $Q$ is shown in Fig. 5(h). When operating at lower frequency with a larger $l$, a higher level of $Q$ can be achieved. The height $d$ is also an important parameter for tailoring this equivalent inductance. As shown in Figs. 5(i) and 5(j), the magnitude of reactance and the resistance both increase with rising frequency at a given fixed $d$. When we fix the frequency at a given value, the magnitude of reactance increases with increasing $d$, and can be explained by Eq. (2); and the equivalent resistance also increases with increasing $d$, due to the larger aperture for radiation leakage at the open boundaries. As is evident from Eq. (4), the equivalent inductance is almost linearly proportional to $d$, as shown in Fig. 5(k), and almost constant vs frequency when we fix $d$. In Fig. 5(l), the variation of $Q$ with different $d$ and frequency is not obvious, but still a high level of $10^2$–$10^3$ can be achieved. The diameter $t$ of the hole on the top PEC plate is chosen according to the dimension of the connecting coaxial cable, and its effect is also studied. As shown in Figs. 5(m) and 5(n), both the magnitude of reactance and equivalent resistance increase with rising frequency at a fixed $t$. At a given frequency, the magnitude of reactance increases with increasing $t$, because the effective area $A$ in formula (2) decreases. But the equivalent resistance almost stays the same with different $t$, due to the little energy leakage from the hole on the top PEC plate. As shown in Fig. 5(o), the inductance is constant as a function of frequency for a given $t$, and increases with increasing $t$, but not much. As shown in Fig. 5(p), the variation of $Q$ with different $t$ and frequency is not obvious at a high level of $10^3$–$10^4$. The relatively higher $Q$ in such a structure may be explained by considering the fact that this is approximately a closed structure in

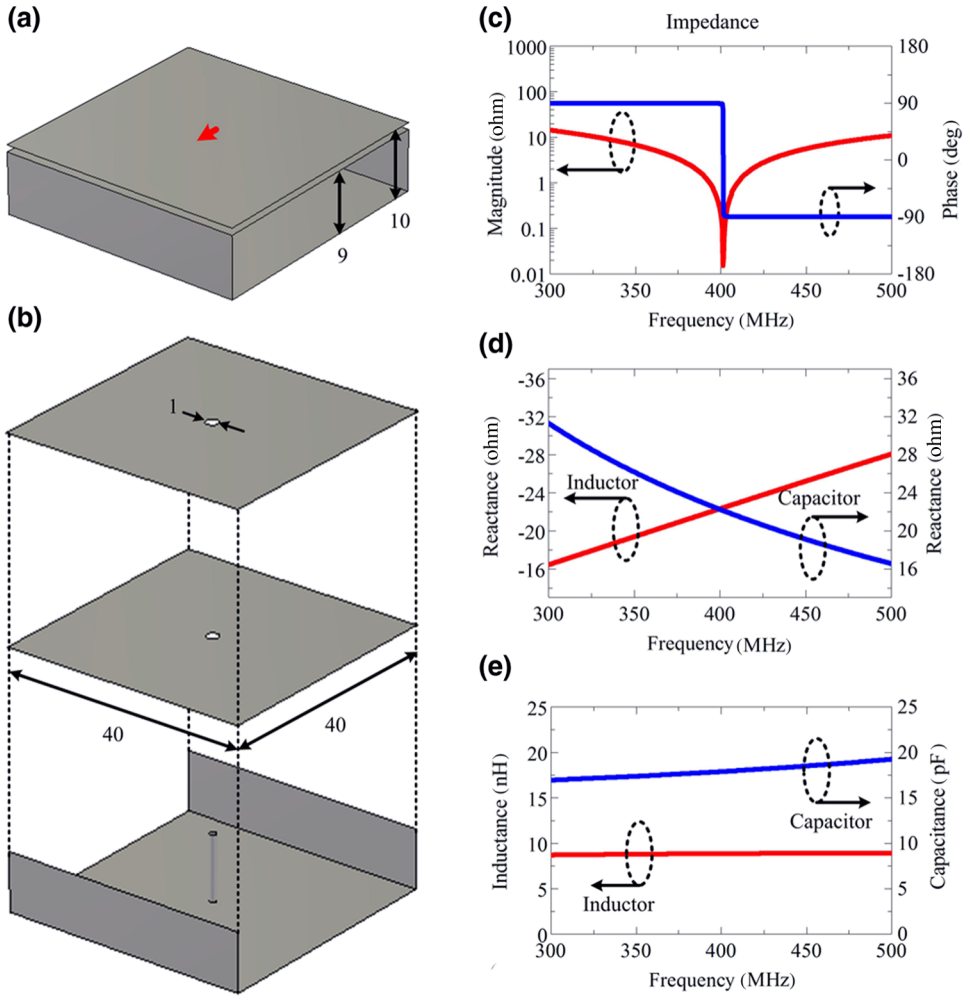


FIG. 6. LC resonator using the proposed inductor and a conventional capacitor. (a) Perspective view, (b) detailed view (when the top plates have been removed in order to show the interior details), and (c) simulation result for the magnitude and phase of the impedance as a function of frequency. (d) Reactance and (e) inductance and capacitance as a function of frequency, for the individual inductor and individual capacitor.

which most of the energy is stored inside the interior empty region. However, the conventional spiral and wound wire inductors are open structures and their wires have ohmic losses, and thus more energy loss is involved. From the above discussion, we list two advantages for the proposed inductors as compared with the conventional wire-based inductors: (1) the inductance is mainly determined by the height, with less effect from the area; and (2) higher $Q$ can be achieved with the closed waveguide structure here. We should also point out that the quantitative values of equivalent inductance for this inductor are in the range of nH, a reasonable value in this range of operating frequencies.

A question may naturally arise: Can these results be obtained using the conventional short-circuited transmission lines? It is well known that by shorting the end of a parallel-wire transmission line, the impedance at the input port is inductive if the electric length of the transmission line is shorter than a quarter wavelength. When we view the structure under study in Fig. 2(d), one can at first treat this inductor as two shorted transmission lines with the length $a/2 \ll \lambda$ in the $x$-$y$ plane connected in parallel in the middle. From the theory of transmission lines, the input impedance of these two parallel-connected shorted transmission lines can be expressed as

$$Z = -iZ_0\tan(\beta a/2)/2, \tag{6}$$

where $Z_0$, $\beta$, and $a$ are characteristic impedance, phase constant, and length of the transmission line, respectively. Due to the subwavelength condition, $\beta a/2 \approx 0$, we can write

$$Z = -iZ_0\tan(\beta a/2)/2 \approx -iZ_0\beta a/4. \tag{7}$$

Since $Z = -i\omega L$, the inductance can be expressed as

$$L \approx Z_0\beta a/4/\omega = aZ_0\sqrt{\varepsilon_0 u_0}/4, \tag{8}$$

showing $L$ to be proportional to $a$ linearly. However, as shown in Fig. 5(c), the equivalent inductance in our structure, while it may increase with $a$, is *not* linearly proportional to $a$. The difference can be attributed to the mode distribution of field in the $y$-$z$ plane inside the structure. In the transmission lines, when the length $a$ is much smaller than the operating wavelength, the voltage (and

electric field) varies almost linearly along the transmission line. But the electric-field distribution of ($TE_{10}$) mode inside our structure, as shown in Figs. 2(e) and 4(a), varies sinusoidally with $y$ and evanescently with $z$ regardless of how small $a$ is, which is different from the case of the transmission line. Considering Eq. (3), we note that a larger value of $a$ results in reduction of the absolute value of the effective negative permittivity $\epsilon_{\text{eff}}$. However, the effective area $A$ increases as $a$ increases. Since both quantities, $\epsilon_{\text{eff}}$ and $A$, are in the denominator, the equivalent inductance does *not* vary linearly with $a$, a different feature than what can be obtained from the transmission line theory.

It is also worth noting that in the waveguide community it is the well-known that a metallic post in a waveguide exhibits inductive reactance [20,21]. However, the formulation for such an inductive post is for the propagating dominant mode in waveguides—different from our proposed structure, which exhibits inductance for the scenario far below cutoff.

Finally, as an example of application of this capacitor-inspired metamaterial inductor, we study an $LC$ resonator with subwavelength dimension, as shown in Fig. 6. The resonator consists of the proposed inductor, connected to a capacitor placed on top of it [Fig. 6(a)]. Due to similarity of structures of both elements, the capacitor is designed by adding another PEC plate above the top PEC plate of the inductor, as shown in Fig. 6(a). The detailed configuration of the model for simulation is illustrated in Fig. 6(b) (where the plates have been separated to show the internal structure and dimensions). Given the values of parameters $a$ and $l$, the resonance frequency can be tailored by changing the heights of the inductor and capacitor. The impedance of the $LC$ resonator as a function of frequency, evaluated from our numerical simulation, is shown in Fig. 6(c), with the magnitude (expressed in red) and the phase (shown in blue). The resonator resonates at 401.2 MHz, at which the magnitude of impedance is minimum as a short circuit, and the phase of impedance goes through a shift from 90° to −90°. For frequencies lower than 401.2 MHz, the phase of current is 90° ahead of the phase of voltage, thus behaving capacitively. For frequencies higher than 401.2 MHz, the phase of current is 90° behind the phase of voltage, thus the circuit acts inductively, in full agreement with a typical series $LC$ resonator. In order to confirm the results, the inductance of the inductor and the capacitance of the capacitor are calculated separately, as shown in Figs. 6(d) and 6(e). The reactance of the inductor is negative and the magnitude increases with the increasing frequency. But the reactance of the capacitor is positive and decreases with the increasing frequency. As illustrated in Fig. 6(d), two reactance curves cross at the frequency of 399.6, which agrees well with the $LC$ resonator simulation. In the frequency band of 300–500 MHz, as shown in Fig. 6(e), the inductance of the inductor with $a = 40$, $l = 40$, and $d_L = 9$ mm is from 8.93 to 8.72 nH. The capacitance of the capacitor with $a = 40$, $l = 40$ , and $d_C = 1$ mm ranging from 17.0 to 19.2 pF. Therefore, the calculated resonance frequency using the standard formula $\omega = 1/\sqrt{\text{LC}}$ is around 399.6 MHz, which agrees well with the simulation result of 401.2 MHz. The overall dimension of the $LC$ resonator shown in Fig. 6(a) is in a subwavelength scale, with the values of $a = l = 40$ mm (0.053λ at 401.2 MHz) and $d_L + d_C = 10$ mm (0.013λ at 401.2 MHz).

## V. CONCLUSIONS

In conclusion, a geometrically simple rf and microwave lumped capacitor-inspired metamaterial inductor is proposed by bringing the notion of optical metatronics back into the rf and microwave domain. Based on this design strategy, the inductance is mostly determined by the inductor height and less dispersive with the operating frequency, and can be evaluated in a way analogous with the capacitor. A relatively higher quality factor can be achieved with this closed structure, different from the conventional inductors made of spiral and wound wires. This component may offer potential applications for the subwavelength integrated resonators in rf and microwave domain.

## FUNDING

This work was supported in part by the US Office of Naval Research (ONR) Multidisciplinary University Research Initiative (MURI) Grant No. N00014-10-1-0942. Y. Li is partially supported by the National Natural Science Foundation of China (NSFC) under Grant No. 61771280.

[1] C. K. Alexander and M. N. O. Sadiku, *Fundamentals of Electric Circuits* (McGraw-Hill, New York, 2013), 5th ed.
[2] H. Greenhouse, Design of planar rectangular microelectronic inductors, IEEE Trans. Parts Hybrids Packag. **10**, 101 (1974).
[3] K. Cheng, Calculation of winding losses in high-frequency toroidal inductors using single strand conductors, IEE Proc. - Electr. Power Appl. **141**, 52 (1994).
[4] X. Mao, W. Chen, and Y. Li, Winding loss mechanism analysis and design for new structure high-frequency gapped inductor, IEEE Trans. Magn. **41**, 4036 (2005).
[5] J. R. Long and M. A. Copeland, The modeling, characterization, and design of monolithic inductors for silicon RF IC's, IEEE J. Solid-State Circuits **32**, 357 (1997).
[6] C. P. Yue and S. S. Wong, On-chip spiral inductors with patterned ground shields for Si-based RF IC's, IEEE J. Solid-State Circuits **33**, 743 (1998).
[7] C. P. Yue and S. S. Wong, Physical modeling of spiral inductors on silicon, IEEE Trans. Electron Devices **47**, 560 (2000).
[8] P. Pieters, K. Vaesen, S. Brebels, S. F. Mahmoud, W. De Raedt, E. Beyne, and R. P. Mertens, Accurate modeling of high-Q spiral inductors in thin-film multilayer

technology for wireless telecommunication applications, IEEE Trans. Microw. Theory Tech. **49**, 589 (2001).

[9] S. Jenei, B. K. J. C. Nauwelaers, and S. Decoutere, Physics-based closed-form inductance expression for compact modeling of integrated spiral inductors, IEEE J. Solid-State Circuits **37**, 77 (2002).

[10] K.-Y. Lee, S. Mohammadi, P. K. Bhattacharya, and L. P. B. Katehi, Compact models based on transmission-line concept for integrated capacitors and inductors, IEEE Trans. Microw. Theory Tech. **54**, 4141 (2006).

[11] N. Engheta, Circuits with light at nanoscales: Optical nanocircuits inspired by metamaterials, Science **317**, 1698 (2007).

[12] N. Engheta, A. Salandrino, and A. Alù, Circuit Elements at Optical Frequencies Nanoinductors, Nanocapacitors, and Nanoresistors, Phys. Rev. Lett. **95**, 095504 (2005).

[13] Y. Sun, B. Edwards, A. Alù, and N. Engheta, Experimental realization of optical lumped nanocircuits at infrared wavelengths, Nat. Mater. **11**, 208 (2012).

[14] H. Caglayan, S.-H. Hong, B. Edwards, C. R. Kagan, and N. Engheta, Near-Infrared Metatronic Nanocircuits by Design, Phys. Rev. Lett. **111**, 073904 (2013).

[15] A. Alù and N. Engheta, All Optical Metamaterial Circuit Board at the Nanoscale, Phys. Rev. Lett. **103**, 143902 (2009).

[16] A. Alù and N. Engheta, Input Impedance, Nanocircuit Loading, and Radiation Tuning of Optical Nanoantennas, Phys. Rev. Lett. **101**, 043901 (2008).

[17] A. Alù and N. Engheta, Tuning the scattering response of optical nanoantennas with nanocircuit loads, Nat. Photonics **2**, 307 (2008).

[18] W. Rotman, Plasma simulation by artificial dielectrics and parallel-plate media, IRE Trans. Antennas Propag. **10**, 82 (1962).

[19] B. Edwards, A. Alù, M. E. Young, M. Silveirinha, and N. Engheta, Experimental Verification of Epsilon-Near-Zero Metamaterial Coupling and Energy Squeezing Using a Microwave Waveguide, Phys. Rev. Lett. **100**, 033903 (2008).

[20] R. E. Collin, *Foundations for Microwave Engineering* (IEEE-Wiley, New York, 2001), 2nd ed.

[21] N. Marcuvitz, *Waveguide Handbook* (McGraw-Hill, New York, 1951), 1st ed.